Modelling Simul. Mater. Sci. Eng. **15** (2007) 619–637 doi:10.1088/0965-0393/15/6/003

Finite element simulation of texture evolution and Swift effect in NiAl under torsion

Thomas Böhlke[1,6], Rainer Glüge[2], Burghardt Klöden[3], Werner Skrotzki[4] and Albrecht Bertram[5]

[1] Universität Karlsruhe (TH), Fakultät für Maschinenbau, Institut für Technische Mechanik, Postfach 6980, D-76128 Karlsruhe, Germany
[2] Otto-von-Guericke Universität Magdeburg, Fakultät für Maschinenbau, Institut für Mechanik, PostFach 4120, D-39016 Magdeburg, Germany
[3] Fraunhofer Institut für Fertigungstechnik and Angewandte Materialforschung, Winterbergstr. 28, D-01277 Dresden, Germany
[4] Technische Universität Dresden, Institut für Strukturphysik, D-01062 Dresden, Germany,
[5] Otto-von-Guericke Universität Magdeburg, Fakultät für Maschinenbau, Institut für Mechanik, PostFach 4120, D-39016 Magdeburg, Germany

E-mail: boehlke@itm.uni-karlsruhe.de, rainer.gluege@masch-bau.uni-magdeburg.de, burghardt.kloeden@ifam-dd.fraunhofer.de, werner.skrotzki@physik.tu-dresden.de and albrecht.bertram@masch-bau.uni-magdeburg.de

Received 17 January 2007, in final form 15 May2007
Published 25 July 2007
Online at stacks.iop.org/MSMSE/15/619

Abstract

The texture evolution and the Swift effect in NiAl under torsion at 727 °C are studied by finite element simulations for two different initial textures. The material behaviour is modelled by an elastic-viscoplastic Taylor model. In order to overcome the well-known shortcomings of Taylor's approach, the texture evolution is also investigated by a representative volume element (RVE) with periodic boundary conditions and a compatible microstructure at the opposite faces of the RVE. Such a representative volume element takes into account the grain morphology and the grain interaction. The numerical results are compared with experimental data. It is shown that the modelling of a finite element based RVE leads to a better prediction of the final textures. However, the texture evolution path is not accounted for correctly. The simulated Swift effect depends much more on the initial orientation distribution than observed in experiment. Deviations between simulation and experiment may be due to continuous dynamic recrystallization.

[6] Author to whom any correspondence should be addressed.

1. Introduction

The intermetallic compound NiAl is of great interest for high-temperature applications since it has a high melting point, a low density, a good corrosion resistance and a moderate creep strength. Until now NiAl has not been applied as a structural material due to the inadequate low-temperature toughness and ductility. Attempts to increase the ductility of NiAl by alloying have not been successful (Noebe *et al* 1993). Alternatively, the mechanical properties can be modified by changing the microstructure using thermo-mechanical processing which induces specific grain size distributions and crystallographic textures (Skrotzki *et al* 2003). Therefore, it is of significant importance to understand the mechanisms of texture formation and grain interactions during the deformation. In this paper we focus on the understanding of the crystallographic texture evolution in NiAl under torsion and the corresponding evolving mechanical anisotropy.

The texture development and the mechanical anisotropy in NiAl are analysed numerically by the finite element method. From the numerical point of view, the actual challenge is to simultaneously describe the mechanical behaviour on two scales, i.e. the grain scale and the macroscale. This is done by adopting Taylor's assumption (Taylor 1938) that the grains deform homogeneously. As a result, the stress in a material point can be computed as the arithmetic mean of the stresses of a finite number of crystallites. The shortcomings of the Taylor model are well known. Usually it gives only reasonable predictions of the texture evolution in single-phase polycrystals. Furthermore, the texture sharpness is significantly overestimated. In order to make more reliable predictions for the texture development we also model a representative volume element (RVE) of NiAl by finite elements. By the RVE approach the grain morphology and the grain interaction are taken into account. The numerical results obtained by these two approaches are compared with experimental data by Skrotzki *et al* (2003). Skrotzki *et al* performed free-end torsion experiments with cylindrical specimens at 727 °C and determined the local crystallographic texture along the radial direction of the cylindrical torsion sample, i.e. as a function of shear strain, with high-energy synchrotron radiation. Due to different processing histories the specimens had two different initial textures, determined globally by neutron diffraction of the whole torsion sample. Both of them were approximate fibre textures. In one case the $\langle 1\,0\,0\rangle$ direction, in the other case the $\langle 1\,1\,1\rangle$ is parallel to the torsion axis. As a result of this comparison, we will learn whether an elastic plastic material model that incorporates the slip system activity combined with the Taylor homogenization scheme is applicable for the simulation of the texture evolution in NiAl. Basically, the lack of other important physical mechanisms that contribute to the texture evolution as well as the rather simple homogenization technique are the main sources of expected disagreements between experimental findings and simulations. In order to estimate the error from the Taylor homogenization we compare the corresponding simulations with results from the more elaborated RVE technique. Any further discrepancy that is eventually found stems therefore from the lack of known texture evolution mechanisms in the material model, like dynamic recrystallization discussed later on.

The outline of the paper is as follows: in section 2 we describe the crystal plasticity model which is used to model the mechanical behaviour on the grain scale. Section 3 briefly describes the two homogenization schemes applied in this paper. In section 4 the numerical results are discussed. The paper closes with a summary.

Notation and pole figure layout. Throughout the text a direct tensor notation is preferred. The scalar product and the dyadic product are denoted by $\boldsymbol{A}\cdot\boldsymbol{B} = \operatorname{tr}(\boldsymbol{A}^{\mathrm{T}}\boldsymbol{B})$ and $\boldsymbol{A}\otimes\boldsymbol{B}$, respectively. Traceless tensors are designated by a prime, e.g. $\boldsymbol{A}'$. A superimposed bar indicates that the

quantity corresponds to the macroscale. All pole figures are stereographic projections of the $\langle 1\,0\,0\rangle$ lattice base vectors into the cross section of the cylindrical torsion samples. The sample coordinate system is chosen with the shear direction horizontal, transverse direction vertical and the shear plane coinciding with the sheet plane normal. The corresponding shear strain γ and the maximum intensity denoted by I (in multiples of a random orientation distribution) are given in each figure caption.

2. Crystal plasticity model

2.1. Elastic law

In the following we rely on the multiplicative decomposition of the deformation gradient $\boldsymbol{F}$ into an elastic part $\boldsymbol{F}_\mathrm{e}$ and a plastic part $\boldsymbol{F}_\mathrm{p}$ (see, e.g. Mandel 1974, Krawietz 1986)

$$\boldsymbol{F} = \boldsymbol{F}_\mathrm{e}\boldsymbol{F}_\mathrm{p}. \tag{1}$$

The plastic deformation is assumed to be volume preserving such that $\boldsymbol{F}_\mathrm{p}$ is unimodular, i.e. its determinant is equal to one. Issues of the non-uniqueness of the decomposition are not addressed here since they are not relevant in this context. It is only mentioned that for a rate-independent behaviour the decomposition can be derived from the concept of material isomorphisms (Bertram 1999, 2005). Such an approach also allows for a precise analysis of the non-uniqueness of the decomposition.

Since the elastic strains in NiAl are small, each linear relation between generalized stress and strain measures is applicable for the description of the elastic behaviour. We assume a linear relation between the 2nd Piola–Kirchhoff stress tensor and Green's strain tensor in the undistorted configuration. In an Eulerian setting this assumption implies that the Kirchhoff stress tensor $\boldsymbol{\tau}$ is given as a linear map of the Almansi strain tensor (see e.g. Böhlke and Bertram 2001)

$$\boldsymbol{\tau} = \mathbb{C}_\mathrm{e}[\boldsymbol{E}^A_\mathrm{e}], \qquad \boldsymbol{E}^A_\mathrm{e} = \frac{1}{2}(\boldsymbol{I} - \boldsymbol{F}_\mathrm{e}^{-\mathrm{T}}\boldsymbol{F}_\mathrm{e}^{-1}), \tag{2}$$

with $\boldsymbol{I}$ being the unit tensor. The Kirchhoff stress $\boldsymbol{\tau}$ is defined by the Cauchy stress tensor $\boldsymbol{\sigma}$ and the determinant J of $\boldsymbol{F}$ through $\boldsymbol{\tau} = J\boldsymbol{\sigma}$. The Eulerian stiffness operator $\mathbb{C}_\mathrm{e}$ is given by the Rayleigh product of $\boldsymbol{F}_\mathrm{e}$ and the constant reference stiffness tensor $\tilde{\mathbb{C}}$

$$\mathbb{C}_\mathrm{e} = \boldsymbol{F}_\mathrm{e} \star \tilde{\mathbb{C}} = \tilde{C}_{ijkl}(\boldsymbol{F}_\mathrm{e}\boldsymbol{e}_i) \otimes (\boldsymbol{F}_\mathrm{e}\boldsymbol{e}_j) \otimes (\boldsymbol{F}_\mathrm{e}\boldsymbol{e}_k) \otimes (\boldsymbol{F}_\mathrm{e}\boldsymbol{e}_l), \tag{3}$$

where $\tilde{C}_{ijkl}$ are the components of $\tilde{\mathbb{C}}$ with respect to $\boldsymbol{e}_i$. Here and in the subsequent sections a tilde indicates that a quantity is formulated with respect to the undistorted configuration which is characterized by the fact that corresponding symmetry transformations are elements of $SO(3)$ (Truesdell and Noll 1965).

The elasticity tensor can be specified by exploiting the cubic crystal symmetry of NiAl. In this case $\tilde{\mathbb{C}}$ has the following projector representation (Rychlewski and Zhang 1989, Bertram and Olschewski 1991)

$$\tilde{\mathbb{C}} = \sum_{\alpha=1}^{3} \lambda_\alpha \mathbb{P}^C_\alpha \tag{4}$$

with the projectors

$$\mathbb{P}^C_1 = \frac{1}{3}\boldsymbol{I} \otimes \boldsymbol{I}, \qquad \mathbb{P}^C_2 = \mathbb{D} - \mathbb{P}^C_1, \qquad \mathbb{P}^C_3 = \mathbb{I}^S - \mathbb{P}^C_2 - \mathbb{P}^C_1. \tag{5}$$

$\mathbb{I}^S$ is the identity on symmetric 2nd-order tensors. The anisotropic part $\mathbb{D}$ is given by a dyadic product of lattice vectors $\tilde{\boldsymbol{g}}_i$

$$\mathbb{D} = \sum_{i=1}^{3} \tilde{\boldsymbol{g}}_i \otimes \tilde{\boldsymbol{g}}_i \otimes \tilde{\boldsymbol{g}}_i \otimes \tilde{\boldsymbol{g}}_i. \tag{6}$$

The eigenvalues λ_α can be written in terms of the components of $\tilde{\mathbb{C}}$ with respect to the orthonormal lattice vectors $\{\tilde{\boldsymbol{g}}_i\}$ $(i = 1, 2, 3)$: $\lambda_1 = \tilde{\mathbb{C}}_{1111} + 2\tilde{\mathbb{C}}_{1122}$, $\lambda_2 = \tilde{\mathbb{C}}_{1111} - \tilde{\mathbb{C}}_{1122}$ and $\lambda_3 = 2\tilde{\mathbb{C}}_{1212}$. Without loss of generality the reference lattice vectors $\tilde{\boldsymbol{g}}_i$ can be identified with the fixed sample system $\boldsymbol{e}_i$. Such a choice only affects the initial value of $\boldsymbol{F}_\mathrm{p}$.

2.2. Flow rule

We adopt the flow rule from finite crystal viscoplasticity theory which specifies the time evolution of the plastic part $\boldsymbol{F}_\mathrm{p}$ of $\boldsymbol{F}$ in terms of the shear rates $\dot{\gamma}_\alpha$ and the slip system tensors $\tilde{\boldsymbol{M}}_\alpha$

$$\dot{\boldsymbol{F}}_\mathrm{p}\boldsymbol{F}_\mathrm{p}^{-1} = \sum_{\alpha=1}^{N} \dot{\gamma}_\alpha(\boldsymbol{T}'_\mathrm{e}, \tau_\alpha^C)\tilde{\boldsymbol{M}}_\alpha. \tag{7}$$

The shear rates $\dot{\gamma}_\alpha$ are assumed to depend on the resolved shear stresses $\tau_\alpha = \boldsymbol{T}'_\mathrm{e} \cdot \tilde{\boldsymbol{M}}_\alpha$ and the flow stress τ_α^C in slip system α. $\boldsymbol{T}_\mathrm{e} = \boldsymbol{F}_\mathrm{e}^\mathrm{T}\boldsymbol{\tau}\boldsymbol{F}_\mathrm{e}{}^{-\mathrm{T}}$ denotes the Mandel stress tensor. The Schmid or slip system tensors $\tilde{\boldsymbol{M}}_\alpha = \tilde{\mathrm{d}}_\alpha \otimes \tilde{\boldsymbol{n}}^\alpha$ are rank-one tensors, which are defined in terms of the slip directions $\tilde{\boldsymbol{d}}_\alpha$ and the slip plane normals $\tilde{\boldsymbol{n}}^\alpha$. The shear rates $\dot{\gamma}_\alpha$ are related to the resolved shear stresses τ_α by the power law relation

$$\dot{\gamma}_\alpha = \dot{\gamma}_0 \mathrm{sgn}(\tau_\alpha) \left| \frac{\tau_\alpha}{\tau_\alpha^C} \right|^m. \tag{8}$$

The application of this power law is motivated by the fact that NiAl shows a rate-dependent behaviour in the considered temperature range (Kloeden *et al* 2005). Such rate-dependent approaches were proposed by Hutchinson (1976) and Asaro and Needleman (1985). The material parameter m quantifies the strain-rate sensitivity of the material and is assumed to be identical for all slip systems. It is generally temperature dependent and can be estimated by strain rate jump experiments. NiAl forms a single-phase ordered B2-structure based on the body centred cubic lattice. In the considered temperature range the potentially active slip systems are given by the primary slip systems $\{1\,1\,0\}\langle 1\,0\,0\rangle$ and the secondary slip systems $\{1\,1\,0\}\langle 110\rangle$ (Fischer-Bühner 1998). Figure 1 shows the two types of slip systems. Inspection of the Schmid tensors shows that there exist six primary and six secondary systems ($N = 12$). Three primary and two secondary slip systems are linearly independent. The initial value of $\boldsymbol{F}_\mathrm{p}$ is given by the inverse of the initial crystal orientation $\boldsymbol{Q}$. $\boldsymbol{Q}$ is introduced in such a way that it maps a reference basis $\boldsymbol{e}_i$ onto the lattice vectors $\boldsymbol{g}_i$ at time t: $\boldsymbol{g}_i(t) = \boldsymbol{Q}(t)\boldsymbol{e}_i$. If $\boldsymbol{g}_i(t)$ is known, the orthogonal tensor $\boldsymbol{Q}$ can be computed by $\boldsymbol{Q} = \boldsymbol{g}_i(t) \otimes \boldsymbol{e}_i$.

2.3. Hardening law

In the following the primary slip systems $\{1\,1\,0\}\langle 1\,0\,0\rangle$ are identified with the indices $1 \ldots 6$. The secondary slip systems $\{1\,1\,0\}\langle 1\,1\,0\rangle$ have the indices $7 \ldots 12$. The activation of slip on the primary and the secondary systems can be described by the corresponding critical resolved shear stresses of the 12 activatable slip systems $\tau^\mathrm{C}_{1\ldots6} = \tau^{\mathrm{C}\langle 1\,0\,0\rangle}$ and $\tau^\mathrm{C}_{7\ldots12} = \tau^{\mathrm{C}\langle 1\,1\,0\rangle}$. The hardening behaviour has been described by only one isotropic internal variable $\tau^{\langle 1\,0\,0\rangle}$ that represents the resolved shear stress for the six $\{1\,1\,0\}\langle 1\,0\,0\rangle$ slip systems. The critical

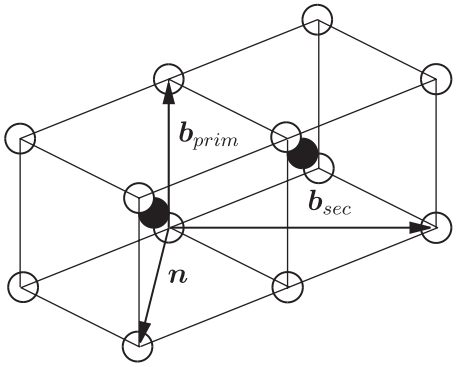

Figure 1. Primary ($\{1\,1\,0\}\langle 1\,0\,0\rangle$) and secondary ($\{1\,1\,0\}\langle 1\,1\,0\rangle$) slip systems in NiAl ($\boldsymbol{n}$: slip plane normal, $\boldsymbol{b}$: Burgers vector).

resolved shear stress for the six $\{1\,1\,0\}\langle 1\,1\,0\rangle$ slip systems is determined based on the assumption $\tau^{C\langle 1\,1\,0\rangle}/\tau^{C\langle 1\,0\,0\rangle} = k = f(T)$. The material parameter k enters the material model as a temperature dependent constant (Miracle 1992). The resolved shear stress $\tau^{\langle 1\,0\,0\rangle}(\gamma)$ is assumed to depend on the total accumulated shear strain in both the primary and the secondary slip systems

$$\gamma = \int \dot{\gamma}\,\mathrm{d}t, \qquad \dot{\gamma} = \sum_{\alpha=1}^{12} |\dot{\gamma}_\alpha|. \tag{9}$$

The function $\tau^{\langle 1\,0\,0\rangle}(\gamma)$ is specified by superimposing the Voce hardening law in a rate-independent fashion and a linear hardening law

$$\tau^{\langle 1\,0\,0\rangle}(\gamma) = \tau_0 + (\tau_\infty - \tau_0)\left(1 - \exp\left(-\frac{\theta_0}{\tau_\infty - \tau_0}\gamma\right)\right) + \theta_\infty \gamma. \tag{10}$$

It is assumed that the cast specimen is not prestrained. The deformation starts at $t = 0$, which yields $\gamma(t = 0) = 0$ as the initial condition for the evolving total accumulated shear strain. The interpretation of the involved hardening parameters is straightforward. $\theta_0 + \theta_\infty$ is the initial slope of the hardening curve and θ_∞ is the asymptotic slope for large γ. τ_0 is the initial critical resolved shear stress and τ_∞ is the asymptotic flow stress of the Voce type part of the hardening law. The aforementioned simplifications are quite crude but are introduced for two reasons. There is only one effective stress–strain curve from a proportional loading test (compression) which can be used for the identification of the hardening parameters. Furthermore, each additional internal variable in the crystal plasticity model increases the numerical costs significantly since a large number of crystal orientations is attached to each integration point of the finite elements in the numerical simulation discussed later.

3. Finite element simulation of texture evolution in NiAl

3.1. Kinematics of torsion and simple shear

A simple shear deformation is defined kinematically by the deformation gradient $\boldsymbol{F} = \boldsymbol{I} + \gamma \boldsymbol{d} \otimes \boldsymbol{n}$ where $\boldsymbol{d}$ and $\boldsymbol{n}$ denote the shear direction and the shear plane normal, respectively. γ is the shear number. The simple shear deformation is a homogeneous deformation. In contrast to simple shear, torsion is an inhomogeneous deformation mode. The corresponding deformation

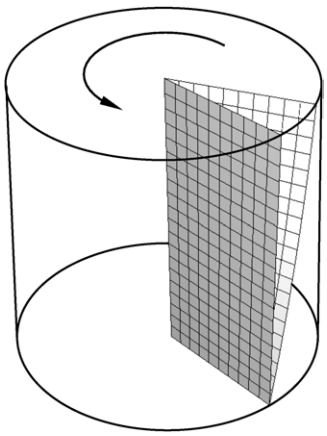

Figure 2. Deformed finite element mesh in an intermediate state of torsion deformation.

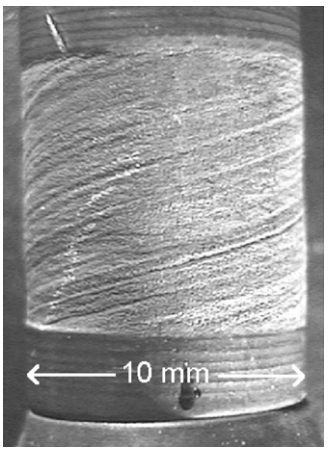

Figure 3. Torsion-deformed cylindrical specimen after one revolution. The marker lines were vertical before deformation (Skrotzki *et al* 2002).

gradient (fixed-end torsion, no axial straining) can be written as $\boldsymbol{F} = \boldsymbol{Q}(\phi)(\boldsymbol{I} + \gamma \boldsymbol{d}(\Phi) \otimes \boldsymbol{n})$. Here the shear number γ is given by $\gamma = RD$, where R denotes the initial radius of the material point and D the twist of the circular specimen. Φ is the angle (cylindrical coordinates) of the material point in the undeformed placement and $\phi = \Phi + DZ$ is the corresponding angle in the deformed placement. Z is the axial coordinate of a material point. $\boldsymbol{Q}(\phi)$ is a proper orthogonal tensor which turns vectors around $\boldsymbol{n}$ with angle ϕ. The shear direction is parallel to the circumference of the cylinder, whereas the shear plane normal is aligned with the cylinder axis of the specimen. Hence torsion is the composition of a position-dependent local simple shear deformation and a rotation. When performing the RVE simulations we will take advantage of this fact.

3.2. Specimen geometry and boundary conditions

The diameter and the length of the cylindrical specimens are both 10 mm. In the experiment the boundary conditions are such that the plane surfaces perpendicular to the cylinder axis

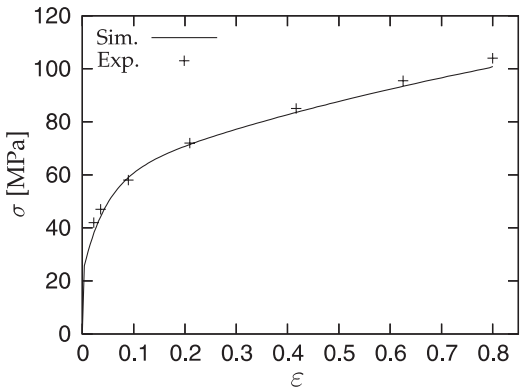

Figure 4. Experimental and simulated equivalent stress σ versus true strain ε (uniaxial compression, $\dot{\varepsilon} = 10^{-4}\mathrm{s}^{-1}$, $T = 700\,^{\circ}\mathrm{C}$, Fischer-Bühner (1998)).

are parallel during the deformation process. The cylinder can freely elongate and contract in the axial and the radial direction. The revolution of the bottom plane of the cylinder is equal to zero. The other top plane undergoes one revolution in 15 000 s which corresponds to a maximum shear rate at the outer surface of $2 \times 10^{-4}\,\mathrm{s}^{-1}$ and a maximum final shear strain of approximately π. Figure 3 shows an experimentally deformed cylindrical specimen. Note that the discretization shown in figure 2 could be replaced by a discretization of one row of elements along the axial direction, since due to the boundary conditions no gradients along this direction are induced.

3.3. Material parameters

The elastic constants are taken from Miracle (1992). The temperature-dependent strain-rate sensitivity parameter m and the ratio of the critical resolved shear stresses $k = \tau^{\mathrm{C}\langle 1\,1\,0\rangle}/\tau^{\mathrm{C}\langle 1\,0\,0\rangle}$ are given by Fischer-Bühner (1998). The hardening parameters have been identified by a Taylor type texture simulation of a uniaxial compression compared with experimental data documented by Fischer-Bühner (1998). Due to the fact that the parameters are defined on the grain scale while the experimental data specify macroscopic quantities, an inverse identification problem has to be solved. The initial texture is discretized by a set of 900 uniformly distributed crystal orientations in order to approximate an almost isotropic crystal orientation distribution that is found in cast, forged and annealed NiAl. The maximum axial true strain is -0.8, while the true strain rate is $10^{-4}\,\mathrm{s}^{-1}$. The identification of the material parameters is done by the trial-and-error method. The comparison of the experimental stress–strain curve with the numerical results can be seen in figure 4. $\theta_0 + \theta_\infty$ mainly influences the initial slope of the effective hardening curve. θ_∞ dominates the asymptotic slope for large strains. Together with the Taylor factor (for the definition in the context of a rate-dependent behaviour see, e.g. Böhlke 2004) τ_0 determines the initial flow stress. τ_∞ influences the asymptotic yield stress in the absence of a linear hardening. The material parameters are given in table 1.

3.4. Initial texture

Due to different processing histories the specimens have two different initial textures. In one case a complete fibre texture with the $\langle 1\,1\,1\rangle$ crystal direction coaxial to the cylinder axis ($\langle 1\,1\,1\rangle$ sample) can be observed. In the other case, the initial texture can be described by a partial $\langle 1\,0\,0\rangle$ fibre with the $\langle 1\,0\,0\rangle$ direction being coaxial to the cylinder axis ($\langle 1\,0\,0\rangle$ sample).

Table 1. Mechanical material parameters of NiAl at 700 °C.

Elastic law	C_{1111}	(GPa)	188
	C_{1122}	(GPa)	123
	C_{1112}	(GPa)	93
Flow rule	$\dot{\gamma}_0$	(s^{-1})	10^{-3}
	m	—	13
	$\tilde{\boldsymbol{M}}_\alpha$	—	$\{1\,1\,0\}\langle 1\,0\,0\rangle$, $\{1\,1\,0\}\langle 1\,1\,0\rangle$
	k	—	2
Hardening rule	τ_0	(MPa)	12
	τ_∞	(MPa)	27
	θ_0	(MPa)	120
	θ_∞	(MPa)	12.5

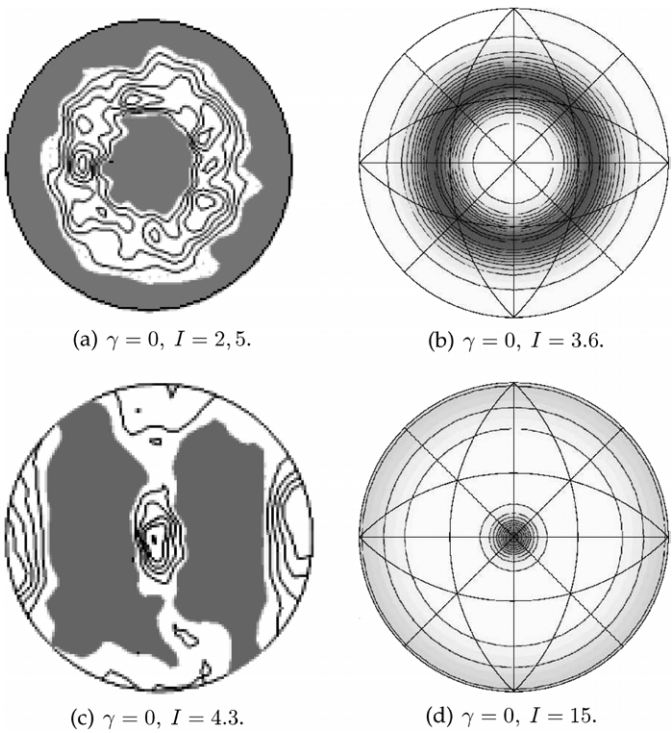

Figure 5. Initial textures in experiment (Skrotzki *et al* 2002) and simulation. Experiment: (*a*) $\langle 1\,1\,1\rangle$ sample, (*c*) $\langle 1\,0\,0\rangle$ sample. Simulation: (*b*) $\langle 1\,1\,1\rangle$ sample, (*d*) $\langle 100\rangle$ sample.

Experimental $\langle 1\,0\,0\rangle$ pole figures are shown in figures 5(*a*) and (*c*).

The initial textures in the NiAl samples are approximated by discrete sets of single crystals. The fibres are generated by aligning a reference crystal such that the $\langle 1\,1\,1\rangle$ or the $\langle 1\,0\,0\rangle$ direction is parallel to the torsion axis. Then a set of crystals approximating the fibre is obtained by rotating the reference crystal around the fibre axis. The distance to the nearest neighbours is constant. Although the $\langle 1\,0\,0\rangle$ sample shows only a partial fibre, the texture is approximated by assuming it would be complete. This approximation has the advantage that

the problem becomes axisymmetric as discussed below in detail. Note that the ⟨1 1 1⟩ and the ⟨1 0 0⟩ fibres have a three- and a four-fold symmetry, respectively. As a result, the crystals are rotated only in the range of 120° and 90°. Both fibres are approximated by 100 single crystals (see figures 5(*b*) and (*d*)). The pole figures corresponding to the numerical results are generated by a superposition of Mises–Fischer distribution functions (Matthies 1980), the mean values of which are determined by the discrete orientations used in the Taylor model. The half-width is equal to 20°.

Fibre textures induce a transversely isotropic material behaviour. Because of the axisymmetry of the specimen shape and the transversely isotropic material behaviour the boundary value problem is axisymmetric. Note that the anisotropy of the material and the twist induced by the boundary conditions imply that one deals with a general axisymmetric state, i.e. the stress state is fully three-dimensional. The modelling of the torsion test in an axisymmetric setting leads to a significant reduction of the number of internal variables involved in the solution of the boundary value problem.

3.5. Finite element simulation of free-end torsion based on the Taylor model

The aim is to perform a finite element simulation on the macroscale, i.e. to simulate the torsion of a circular bar, and simultaneously to take into account the crystallographic texture on the grain scale. The relation between the macroscopic and mesoscopic stress and strain measures can be determined, e.g. based on Taylor type models (Taylor 1938, Asaro and Needleman 1985). The Taylor model assumes a homogeneous deformation field through the microstructure of polycrystals. It, therefore, satisfies the strain compatibility, but not the stress equilibrium at the grain boundaries. The Taylor model gives reasonable qualitative approximations of the crystallographic texture evolution in many single-phase cubic materials, but is known to overestimate the stresses and the texture sharpness significantly. Different approaches have been discussed in the literature in order to improve the full constrained Taylor modelling of the texture evolution. The most simple one is based on a relaxation of certain constraints of the deformation field (RC Taylor models). A typical example is the LAMEL model by van Houtte (1982), which has been developed to predict rolling textures. Roughly speaking, the model takes a stack of two grains, which is compressed, and permits an inhomogeneous deformation. This allows to satisfy the stress equilibrium for the shear stresses within the flattening plane. The disadvantage of the model is that it is only applicable for one specific deformation mode. Although the LAMEL model is a simple grain interaction model (GIA), the term GIA model refers to a more sophisticated model that takes a cell of eight grains into account (Crumbach *et al* 2001). Due to the more complex modelling of the grain interaction, the premises for the texture prediction are better than for the LAMEL model. For a comparison see van Houtte *et al* (2002, 2006). Another quite successful approach is given by the class of self-consistent approximations of the local deformation behaviour (e.g. Molinari *et al* 1987), which satisfy the strain compatibility and the stress equilibrium in an averaged sense. A purely numerical approach for a detailed description of the microstructure is given by the RVE technique based on finite elements and crystal plasticity (Bronkhorst *et al* 1992, Bertram *et al* 1998, Cailletaud *et al* 2003, Kanit *et al* 2003), sometimes referred to as crystal plasticity finite element model (CPFEM). An RVE is a statistically representative volume fraction of the microstructure. Such an approach takes into account the grain morphology and the grain interaction.

If the crystallographic texture has to be taken into account at the integration point level, in most cases Taylor type models are used since they are computationally much less expensive compared with other homogenization schemes. In the simulation of the torsion test we adopt

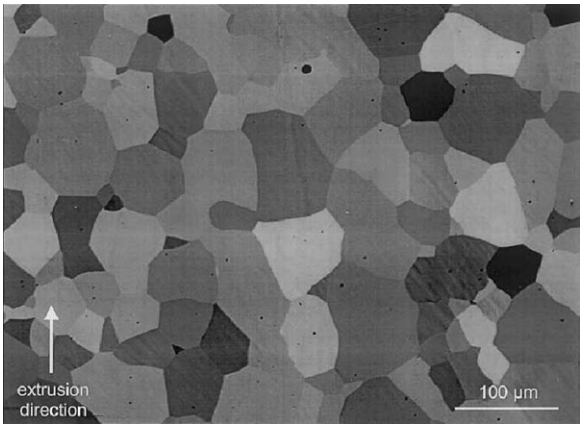

Figure 6. Microstructure of extruded and fully recrystallized NiAl (Skrotzki *et al* 2002).

the Taylor assumption of a homogeneous deformation gradient

$$\boldsymbol{F} = \bar{\boldsymbol{F}}. \tag{11}$$

For statistically homogeneous materials without pores and cracks the effective Kirchhoff stress tensor is given by the volume average over the reference volume V. Assuming that the crystal orientations of the grains are initially homogeneous, the following formula for the effective Kirchhoff stress tensor can be obtained

$$\bar{\boldsymbol{\tau}} = \frac{1}{V}\int_V \boldsymbol{\tau}\ \mathrm{d}V = \sum_{\beta=1}^{M} \nu_\beta \boldsymbol{\tau}_\beta, \tag{12}$$

where ν_β is the (initial) volume fraction of grain β and $\boldsymbol{\tau}_\beta$ is the corresponding Kirchhoff stress tensor. M is the total number of grains.

For the axisymmetric simulation with the commercial finite element code ABAQUS (ABAQUS/Standard 2003) 200 CGAX4 elements are used which describe a general axisymmetric state being fully three dimensional. In figure 2 the deformed finite element mesh is shown for an intermediate state of deformation. The CGAX finite element simulation is performed with 100 crystal orientations per integration point. The boundary conditions are chosen according to the experimental ones discussed above. The differential equations specifying the material model are integrated by applying the implicit Euler method in an incrementally objective setting. The constraint of plastic incompressibility is fulfilled by a projection method.

3.6. Finite element simulation with a representative volume element

For a reliable estimation of the macroscopic mechanical properties, the modelling of the grain interaction and the grain morphology is of significant importance. However, both features are neglected by the Taylor model. In order to obtain better predictions for the texture development, a three-dimensional aggregate of polyhedral shaped NiAl grains is modelled by the RVE approach using the commercial finite element code ABAQUS. Initially, the RVE has the shape of a cube.

The microstructure of NiAl before deformation is shown in figure 6 (Skrotzki *et al* 2002). The initial geometry of the grains in the RVE is idealized by a periodic Poisson–Voronoi

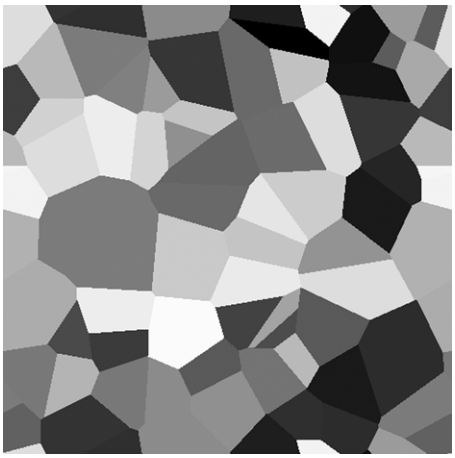

Figure 7. Two-dimensional Poisson–Voronoi structure.

tessellation with 350 grains (see figure 8). This class of tesselations is topologically equivalent to real microstructures in metals. Figure 7 shows a two-dimensional periodic Poisson–Voronoi structure. The crystal orientations are chosen as described above. The displacement fluctuations are assumed to be periodic on the boundary of the RVE. In order to make the implementation of the periodic boundary conditions as simple as possible, the RVE is regularly discretized by $25 \times 25 \times 25 = 15625$ equal-sized C3D8 elements. This Gauss point method (Kanit *et al* 2003) is the most simple meshing technique.

The total number of grains is quite small but allows for a coarse approximation of the crystallographic texture. Due to the fact that periodic boundary conditions are used and that about 44 finite elements are used to discretize one grain, it should be expected that the RVE approach predicts a much softer texture compared with the Taylor model. Since the grains interact and deform inhomogenously, the RVE approach also may predict other texture components than the Taylor model. As discussed before, fixed-end torsion corresponds to the composition of simple shear and a rigid body rotation. Taking this into account, the deformation of any material point of the specimen can be approximated by a simple shear deformation. Note that the axial effects are neglected by this approach. Nevertheless, the plastic anisotropy inducing the axial strains under free-end torsion causes axial stresses in the case of simple shear. These axial stresses are discussed below.

4. Numerical results and discussion

4.1. Texture evolution: simulation versus experiment

4.1.1. Texture evolution: ⟨1 1 1⟩ *sample.* In figure 10 the experimental (1 0 0) pole figures (Skrotzki *et al* (2003)) are shown for the ⟨1 1 1⟩ initial fibre. The fibre axis which is initially aligned parallel to the shear plane normal, rotates around the transverse direction to the shear direction. During this rotation it falls apart and a texture component starts to develop. The component is aligned with its ⟨1 0 0⟩ direction parallel to the shear direction and the ⟨1 1 0⟩ direction parallel to the shear plane normal. Using the notation {shear plane}⟨shear direction⟩ the component is written as {1 1 0}⟨100⟩.

In figure 11 the texture evolution is shown for the CGAX finite element simulation of the free-end torsion experiment at different shear strains. It can be seen that the CGAX finite

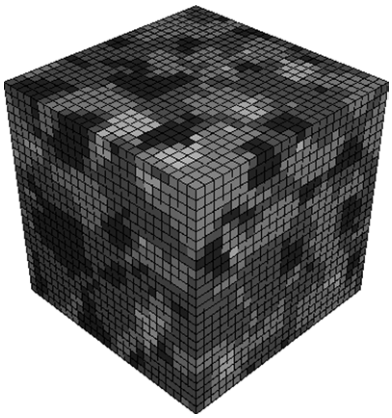

Figure 8. Initial mesh of the RVE with periodic microstructure.

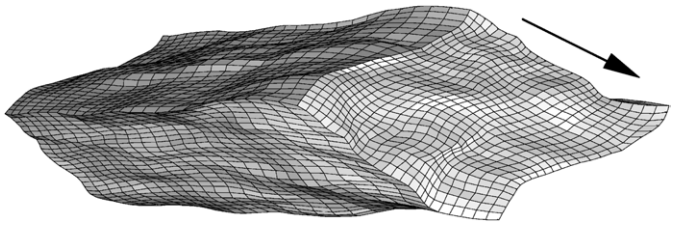

Figure 9. Deformed mesh of the RVE (shear number $\gamma = 2$, the arrow indicates the shear direction, deformation is unscaled).

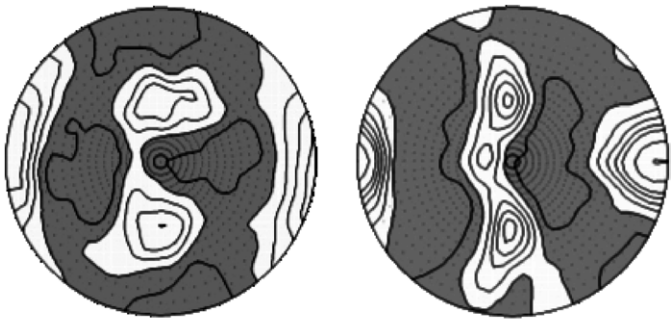

(a) $\gamma = 1.4,\ I = 2.8$ (b) $\gamma = 2.8,\ I = 5.0$

Figure 10. (1 0 0) pole figures of the ⟨1 1 1⟩ sample, experimentally deformed in torsion at different shear strains (Skrotzki *et al* 2003).

element simulation also predicts the $\{1\,1\,0\}\langle 1\,0\,0\rangle$ component, but the development is much slower.

In figure 13(a) comparison of pole figures based on different homogenization schemes for a shear strain of $\gamma = 2$ can be seen. Figure 13(a) shows the prediction of the CGAX finite element simulation of the free-end torsion test. Here, the cylindrical specimen is discretized by finite elements and the stress at the integration points is computed based on the Taylor model. In such a type of simulation the grain scale and the macroscale are linked and the Swift effect

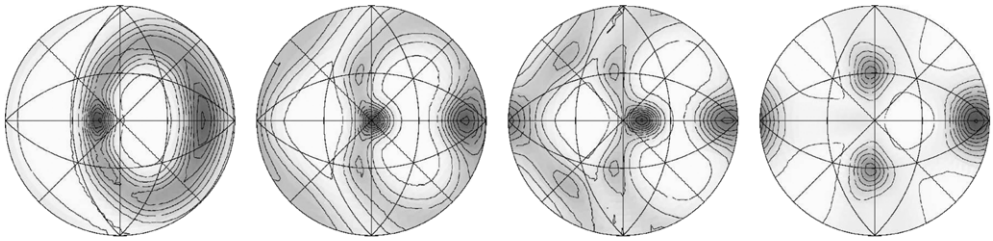

(a) $\gamma = 1.4, I = 5.2$ (b) $\gamma = 2.0, I = 6.7$ (c) $\gamma = 2.8, I = 6.6$ (d) $\gamma = 5.0, I = 10$

Figure 11. (1 0 0) pole figure: FE simulation (free-end torsion, ⟨1 1 1⟩ sample, horizontal axis = SD, vertical axis = TD).

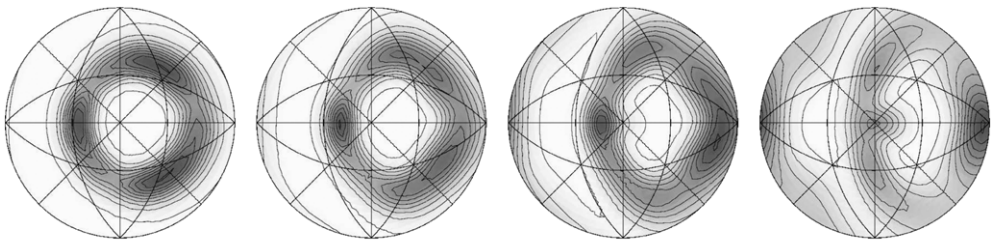

(a) $\gamma = 0.5, I = 4.1$ (b) $\gamma = 1.0, I = 4.5$ (c) $\gamma = 1.5, I = 3.9$ (d) $\gamma = 2.0, I = 4.7$

Figure 12. (1 0 0) pole figure: predicted texture for different stages of deformation (FE based RVE simulation, ⟨1 1 1⟩ sample, simple shear).

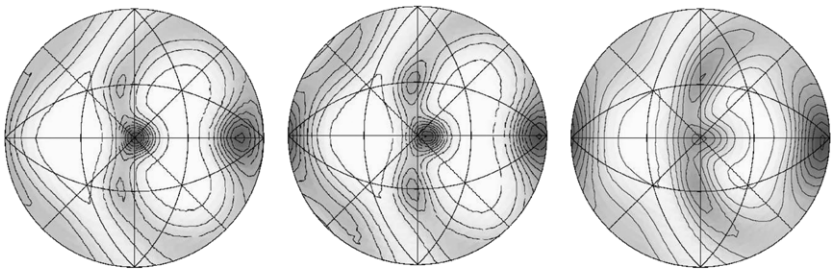

(a) FE simulation (free-end torsion), $I = 6.7$ (b) Taylor simulation (simple shear), $I = 6.3$ (c) RVE simulation (simple shear), $I = 4.7$

Figure 13. (1 0 0) pole figure: comparison of different homogenization techniques, (⟨1 1 1⟩ sample, $\gamma = 2$).

can be analysed numerically. Figure 13(*b*) shows the (1 0 0) pole figure as it is predicted by the Taylor model for a simple shear deformation which neglects the axial strain. The difference between simple shear and torsion has been discussed above. It can be seen that the pole figures are almost identical, which indicates that the axial strain is not of importance for the texture evolution. Figure 13(*c*) shows the prediction of the RVE simulation. The pole figures for subsequent stages of deformation are presented in figure 12. This type of simulation, which takes into account the interactions between the grains, shows a significant difference to the Taylor based simulations. Some texture components predicted by the Taylor simulation are much sharper compared with the ones found in the RVE simulation than others, e.g. the pole

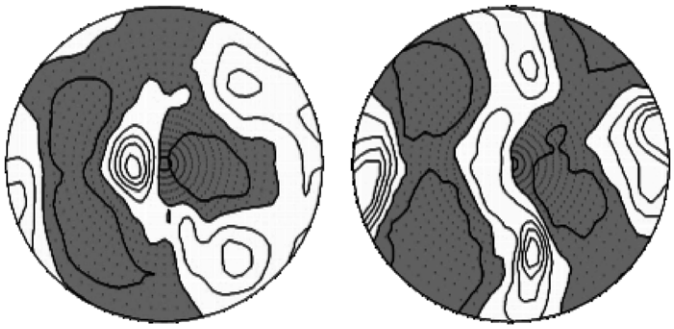

(a) $\gamma = 1.4,\ I = 3.3$ (b) $\gamma = 2.8,\ I = 4.0$

Figure 14. Experimental (1 0 0) pole figure ($\langle 1\,0\,0\rangle$ sample, Skrotzki *et al* 2003).

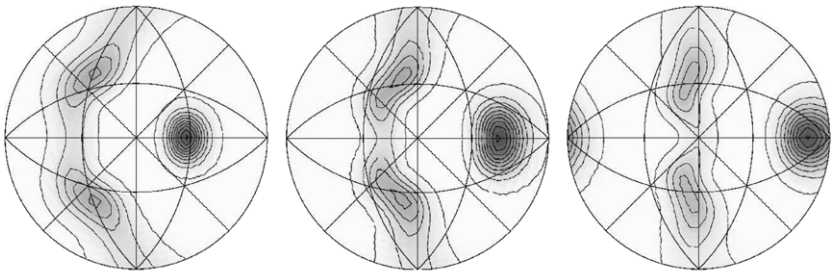

(a) $\gamma = 1.4, I = 11.5$ (b) $\gamma = 2.0, I = 9.8$ (c) $\gamma = 2.8, I = 12.6$

Figure 15. (1 0 0) pole figure: FE simulation (free-end torsion, $\langle 1\,0\,0\rangle$ sample).

found in the shear plane normal direction, which is represented in the centre of the pole figure. The deformed mesh for a shear strain $\gamma = 2$ can be seen in figure 9.

4.1.2. Texture evolution: $\langle 100\rangle$ *sample.* In case of the $\langle 1\,0\,0\rangle$ initial partial fibre, the evolved texture is shown in figure 14 (Skrotzki *et al* 2002). Similar to the other case, during simple shear the fibre falls apart and a $\{1\,1\,0\}\langle 1\,0\,0\rangle$ texture component develops.

In figure 15 the texture evolution of the complete initial fibre is shown for the CGAX finite element simulation of the free-end torsion experiment and different shear strains. It can be seen that the CGAX finite element simulation predicts the $\{1\,1\,0\}\langle 1\,0\,0\rangle$ component. In figure 17 a comparison of the (1 0 0) pole figures based on different homogenization schemes is given for the shear strain $\gamma = 2$. A comparison of the Taylor simulation with the RVE simulation shows that the main difference is the sharpness of the predicted texture, and it seems that the RVE calculation does not predict more texture components than the Taylor simulation (see figure 17). Figure 17(*a*) shows the prediction of the CGAX finite element simulation of the free-end torsion test. Figure 17(*b*) gives the (1 0 0) pole figure as it is predicted by the Taylor model for a simple shear deformation. Again, this simulation indicates that the axial strain is not of significant importance for the texture evolution. In figure 17(*c*) one can see the prediction of the RVE simulation. This simulation also shows a weaker texture. The pole figures for subsequent stages of deformation as predicted by the FE based RVE approach are presented in figure 16. Here one can see that the fibre axis, which initially is aligned parallel to the shear plane normal, rotates around the transverse direction.

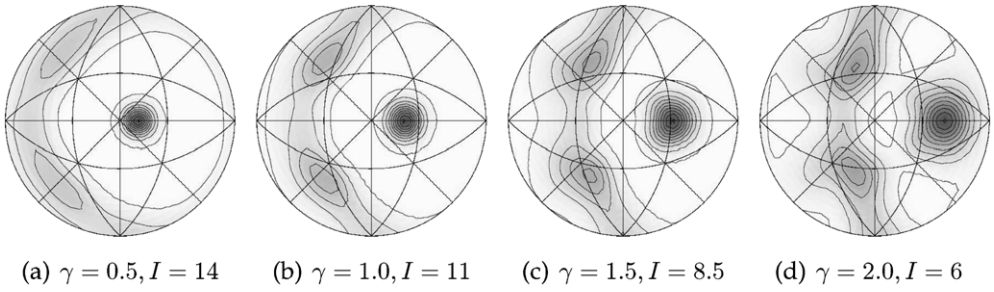

Figure 16. (1 0 0) pole figure: predicted texture for different stages of deformation (FE based RVE simulation, ⟨1 0 0⟩ sample, simple shear).

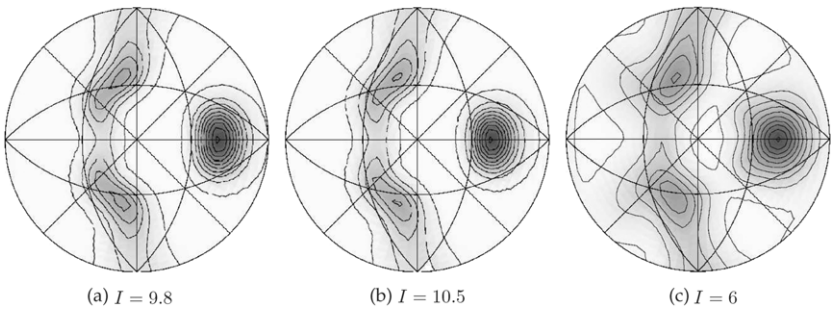

Figure 17. (1 0 0) pole figure: comparison of experiment and simulation (⟨1 0 0⟩ sample, $\gamma = 2$). (*a*) FE simulation (free-end torsion), (*b*) Taylor simulation (simple shear) and (*c*) RVE simulation (simple shear).

4.1.3. General discussion. A comparison of experimental and simulated textures shows that the main texture component {1 1 0}⟨100⟩ is best reproduced by the FE based RVE simulation. However, the texture development under shear strain is not reproduced at all for both initial fibres. In the case of the ⟨111⟩ fibre, the {110}⟨100⟩ component is formed much faster in the experiment. This may be due to continuous dynamic recrystallization (CDRX, see Gourdet and Montheillet (2003)) leading to a change from a low angle grain boundary (LAGB) to a high angle grain boundary (HAGB) structure (Skrotzki *et al* 2003). Simultaneously, limited migration of HAGBs takes place mainly driven by the difference between dislocation densities of the grains located on the two sides of the boundary. On the one hand, besides usual dynamic recovery, this grain boundary migration leads to an absorption of dislocations from the grain interior, i.e. to additional softening. On the other hand, it gives rise to a new grain subdivision by LAGBs, which may develop during further straining to HAGBs. Hence, this continuous process of coarsening, subdivision and shearing yields a steady state microstructure of constant average grain size, aspect ratio and grain shape evolution. These aspects have not been taken into account in the simulations. In the case of the ⟨100⟩ fibre besides the aspects described above, deviations from the ideal fibre may be of influence at low shear strains. Actually, the experimental texture is more of the type of a cube component. In future modelling these aspects have to be taken into account.

4.2. Swift effect

If polycrystals are subjected to finite, monotonic free-end torsion, a significant axial strain can be observed in many materials (Böhlke *et al* 2003). This effect was first described by

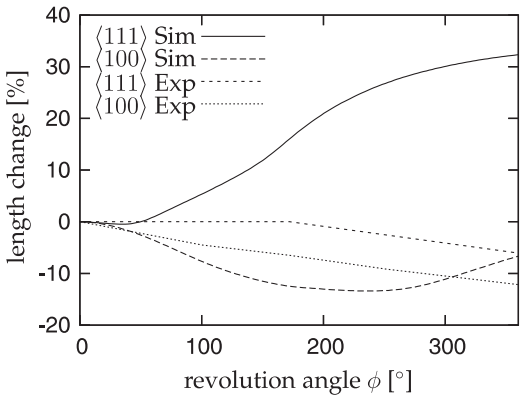

Figure 18. Axial elongation versus angle of revolution observed in experiments and simulations.

Swift (1947), who assumed that hardening mechanisms are responsible for the axial effects. It is generally known as the Swift effect.

Swift (1947) performed his experiments to check whether straight radial lines remain straight. The observations done on mild steel showed a change of the external dimensions under plastic torsion, which was not in accordance with any known plasticity theory. Therefore, similar tests were performed with 70–30 brass, stainless steel, aluminium, 0.5% carbon steel, copper and cupro-nickel with different specimen geometries. All materials and all specimen geometries tended to elongate under severe torsional strain. The axial strain accumulation does not depend on the direction of the torsion. Swift also investigated the influence of prior strain or heat treatment. Similar results have been obtained by Stüwe and Turck (1964), Gil-Sevillano *et al* (1975) and Tóth and Jonas (1989). Swift assumed that the strain hardening causes the axial effects. Billington (1976) contradicted this assumption by experiments. He observed continuous elongations in iron independent of hardening. Nowadays, it has been accepted that the axial effects are due to the crystallographic texture (Montheillet *et al* 1985, Harren *et al* 1989).

The CGAX finite element simulations of the torsion test with NiAl indicate a strong dependence on the axial elongation from the initial orientation distribution. The specimen shortens and lengthens in the case of a ⟨1 0 0⟩ initial fibre and ⟨1 1 1⟩ initial fibre, respectively (see figure 18). A comparison of the simulated and the experimentally observed Swift effect shows that the tendency whether lengthening or shortening occurs, is accounted for in the low-temperature range, where CDRX is less active. However, the length change is strongly overestimated in the simulations. This is due to the extreme assumption of a homogeneous strain field made in the Taylor model. At higher temperatures, even the tendency of the length change cannot be predicted by the Taylor model. This may be due to the neglect of CDRX in the material model. The CDRX (see section 4.1.3) leads to the formation of a cube component which is responsible for shortening and thus compensating the lengthening effect in the ⟨1 1 1⟩ sample.

In the RVE simulation and the Taylor model calculation the deformation mode was a simple shear, therefore no axial straining could be observed. However, it is possible to compare the normal stresses that are induced due to the no-displacement boundary condition in the direction of the shear plane normal. This is plotted in figure 19, where an interval of $0 < \gamma < 2$ is under consideration. One can see that in the case of the ⟨111⟩ fibre the restraining stress is negative, which indicates that a compression stress is needed to maintain the height of the cylindrical

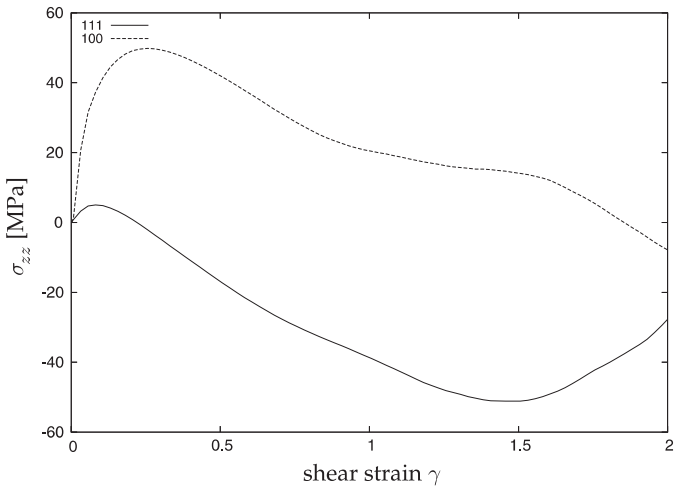

Figure 19. Stress component normal to shear plane in simple shear deformation.

specimen. This means that the sample would elongate, which was found in the CGAX finite element simulations (see figure 18). In the case of the ⟨1 0 0⟩ fibre the sample shortens, which yields positive restraining stresses. In the Taylor model calculations, the maximum absolute restraining stresses are about a factor of 3.5 and 2.2 times the maximum of the absolute restraining stresses from the RVE simulations (in the ⟨1 1 1⟩ sample and the ⟨1 0 0⟩ sample, respectively). This demonstrates the well-known fact that the stresses are overestimated when Taylor's assumption is applied. For the ⟨1 1 1⟩ fibre the overestimation is significantly larger than for the ⟨1 0 0⟩ fibre. This corresponds to the findings that in the case of the ⟨1 1 1⟩ fibre the texture evolution in the Taylor model differs more from the findings of the RVE calculation as in the case of the ⟨1 0 0⟩ fibre.

5. Summary

The texture evolution in NiAl under torsion at 727 °C has been numerically analysed by two different homogenization schemes. In one case the constitutive behaviour of the polycrystalline NiAl is simulated based on Taylor's assumption of a homogeneous deformation on the grain scale. The advantage of this approach is that the texture evolution can be taken into account in finite element simulations of the mechanical behaviour of macroscopic structural components. The disadvantage is that due to the Taylor assumption, the interaction of grains is neglected. In the other case a RVE with several hundred polyhedral shaped grains is modelled based on finite elements. The advantage of this approach is that the interaction of grains is modelled, which is of great importance for the prediction of the texture development and the plastic anisotropy. The disadvantage of the RVE approach is that a direct link to finite element simulations on the macroscale will cause high computational costs. The application of the two schemes allows for an investigation of different aspects of the deformation behaviour of NiAl. The first method bridges the gap between the grain scale and the macroscopic material response. The second approach gives a refined picture of the micromechanical mechanisms. The numerical results are compared with experimental data. The essential results of this investigation are the following: the experimental texture at high shear strains is simulated best by an FE based RVE model. The texture simulations that used the RVE technique reproduce the experiments better than the

models that use the Taylor assumption, which was found as well by van Houtte *et al* (2006). This is not a surprising result. However, the evolution path of the texture is not reproduced correctly. This deficiency might be due to CDRX as well as an insufficient representation of the initial texture in the ⟨1 0 0⟩ sample. The simulated Swift effect depends on the orientation distribution. There is lengthening for samples with a ⟨1 1 1⟩ fibre texture, while samples with a ⟨1 0 0⟩ fibre shorten during free-end torsion. Consequently, in the case of fixed-end torsion, an axial compression or tension occurs, depending on the initial fibre. The latter effect agrees with the experiment. The discrepancy between simulation and experiment is assumed to be caused by CDRX, which even in the ⟨1 1 1⟩ samples produces a certain amount of oblique cube component leading to shortening.

References

ABAQUS/Standard 2003 Hibbitt, Karlsson & Sorensen, Inc.

Asaro R J and Needleman A 1985 Texture development and strain hardening in rate-dependent polycrystals *Acta Metall.* **33** 923–53

Bertram A 1999 An alternative approach to finite plasticity based on material isomorphisms *Int. J. Plast.* **15** 353–74

Bertram A 2005 *Elasticity and Plasticity of Large Deformations* (Berlin: Springer)

Bertram A, Böhlke T and Kraska K 1998 Texture development of aluminum polycrystals under finite plastic deformations *IUTAM-Symp. Micro- and Macrostructural Aspects of Thermoplasticity* ed O Bruhns and E Stein (Dordrecht: Kluwer)

Bertram A and Olschewski J 1993 Zur Formulierung anistroper linear anelastischer Stoffgleichen mit Hilfe einer Projektionsmethode *Z. Angew. Math. Mech.* **73** T401–403

Billington E. 1976 Non-linear mechanical response of various metals: II. Permanent length changes in twisted tubes *J. Phys. D: Appl. Phys.* **10** 533–52

Böhlke T 2004 The Voigt bound of the stress potential of isotropic viscoplastic fcc polycrystals *Arch. Mech.* **56** 423–43

Böhlke T and Bertram A 2001 The evolution of Hooke's law due to texture development in polycrystals *Int. J. Solids Struct.* **38** 9437–59

Böhlke T, Bertram A and Krempl E 2003 Modeling of deformation induced anisotropy in free-end torsion *Int. J. Plast.* **19** 1867–884

Bronkhorst C, Kalidindi S and Anand L 1992 Polycrystalline plasticity and the evolution of crystallographic texture in fcc metals *R. Soc. Lond.* A **341** 443–77

Cailletaud G, Forest S, Jeulin D, Feyel F, Galliet I, Monoury V and Quilici S 2003 Some elements of microstructural mechanics *Comput. Mat. Sci.* **27** 351–74

Crumbach M, Pomana G, Wagner P and Gottstein G 2001 *Proc. 1st Joint Int. Conf. on Recrystallisation and grain growth (Aachen, Germany)* ed G Gottstein and D Molodov

Fischer-Bühner J 1998 *Mechanismen der Mikrostruktur- und Texturentwicklung von Polykristallinem NiAl* (Aachen: Shaker)

Gil-Sevillano J, Van Houtte P and Aernoudt E 1975 Deutung der schertexturen mit Hilfe der Taylor-analyse *Z. Metallk.* **66** 367

Gourdet S and Montheillet F 2003 A model of continuous dynamic recrystallization *Acta Mater.* **51** 2685–99

Harren S, Lowe T, Asaro R and Needleman A 1989 Analysis of large-strain shear in rate-dependent face-centered cubic polycrystals: correlation of micro- and macro-mechanics *Phil. Trans. R. Soc. Lond.* A **328** 443–500

Hutchinson J 1976 Bounds and self-consistent estimates for creep of polycrystalline materials *Proc. R. Soc. Lond.* A **348** 101–27

Kanit T, Forest S, Galliet I, Mounoury V and Jeulin D 2003 Determination of the size of the representative volume element for random composites: statistical and numerical approach *Int. J. Solids Struct.* **40** 3647–79

Kloeden B, Rybacki B, Oertel C-G and Skrotzki W 2005 Torsional creep of polycrystalline NiAl *Scr. Mater.* **52** 289–93

Krawietz A 1986 *Materialtheorie* (Berlin: Springer)

Mandel J 1974 Thermodynamics and plasticity ed J Delgado Domingos *et al Proc. Int. Symp. Foundations of Continuum Thermodynamics* (London: MacMillan)

Matthies S 1980 Standard functions in texture analysis *Phys. Status. Solidi* B **101** K111–15

Miracle D 1992 The physical and mechanical properties of NiAl *Acta Metall. Mater.* **41** 649–84

Molinari A, Canova G and Ahzi S 1987 A self consistent approach of the large deformation polycrystal viscoplasticity *Acta Metall.* **35** 2983

Montheillet F, Gilormini P and Jonas J 1985 Relation between axial stresses and texture development during torsion testing: a simplified theory *Acta Metall.* **33** 705–17

Noebe R, Bowman R and Nathal M 1993 Review of the physical and mechanical properties of the B2 compound NiAl *Int. Mater. Rev.* **38** 193–232

Rychlewski J and Zhang J 1989 Anisotropy degree of elastic materials *Arch. Mech.* **47** 697–715

Skrotzki W, Klöden B, Tamm R, Oertel C-G, Garbe U and Rybacki E 2003 Torsion texture measurements with high-energy synchrotron radiation on NiAl *Textures Microstruct.* **35** 163–73

Skrotzki W, Tamm R, Oertel C-G, Beckers B, Brokmeier H-G and Rybacki B 2002 Influence of texture and hydrostatic pressure on the room temperature compression of nial polycrystalls *Mater. Sci. Eng.* **329–331** 235–40

Stüwe H and Turck H 1964 Zur Messung von Fließortkurven im Torsionsversuch *Z. Metallk.* **55** 699–703

Swift H 1947 Length changes in metals under torsional overstrain *Engineering* **163** 253–7

Taylor G 1938 Plastic strain in metals *J. Inst. Met.* **62** 307–24

Tóth L S and Jonas J J 1989 Analytic prediction of texture and length changes during free-end torsion *Textures Microstruct.* **10** 195–209

Truesdell C and Noll W 1965 The Non-Linear Field Theories of Mechanics (*Encyclopedia of Physics* vol III/3) (Berlin: Springer)

van Houtte P 1982 On the equivalence of the relaxed Taylor theory and the Bishop-Hill theory for partially constrained plastic deformation of crystals *Mater. Sci. Eng.* **55** 69–77

van Houtte P, Delannay L and Kalidini S 2002 Comparison of two grain interaction models for polycrystal plasticity and deformation texture prediction *Int. J. Plast.* **18** 359–77

van Houtte P, Kanjarla A, van Bael A, Seefeldt M and Delannay L 2006 Multiscale modelling of the plastic anisotropy and deformation texture of polycrystalline materials *Eur. J. Mech. A: Solids* **25** 634–48